The Journal of Neuroscience

https://jneurosci.msubmit.net

JN-RM-0251-25R2

Attention alters population spatial frequency tuning

Luis Ramirez, University of California San Diego
Feiyi Wang, Boston University
Sam Ling, Boston University

Commercial Interest:

Title: Attention alters population spatial frequency tuning

Abbreviated title: Attention alters pSFT

Luis D. Ramirez[1,2,*], Feiyi Wang[1,2], & Sam Ling[1,2].

[1] Department of Psychological & Brain Sciences, Boston University, Boston, Massachusetts, 02215.
[2] Center for Systems Neuroscience, Boston University, Boston, Massachusetts, 02215.

***Correspondence:** Luis D. Ramirez (lur003@ucsd.edu).

Number of pages: 38

Number of figures: 4

Number of tables: 2

Number of supplemental figures: 3

Number of supplemental tables: 3

Number of words: abstract = 203, introduction = 515, discussion = 1253

Conflict of Interests: The authors declare no competing financial interests.

Acknowledgments: We thank Emily Wiecek, Jasmine Pan, Minsun Park, David Somers, and Taosheng Liu for thoughtful discussion. We also thank the editors and reviewers for their feedback. This research was funded by National Institutes of Health Grant EY028163 to S. Ling and supported by F99NS124144 to L.D. Ramirez. L.D. Ramirez's current affiliation is with the Department of Psychology at University of California San Diego. This research was carried out at the Boston University Cognitive Neuroimaging Center. This work involved the use of instrumentation supported by the NSF Major Research Instrumentation grant BCS-1625552. We acknowledge the University of Minnesota Center for Magnetic Resonance Research for use of the multiband-EPI pulse sequences. Data was analyzed on a high-performance computing cluster supported by the ONR grant N00014-17-1-2304.

Author Contributions: L.D.R., F.W., and S.L. designed research; L.D.R. and F.W. performed research. L.D.R and F.W. analyzed data; L.D.R., F.W., and S.L. prepared the manuscript.

Abstract

Spatial frequency (SF) selectivity serves as a fundamental building block within the visual system, determining what we can and cannot see. Attention is theorized to augment the visibility of items in our environment by changing how we process SFs. However, the specific neural mechanisms underlying this effect remain unclear, particularly in humans. Here, we used functional magnetic resonance imaging (fMRI) to measure voxel-wise population SF tuning (pSFT), which allowed us to examine how attention alters the SF response profiles of neural populations in early visual cortex (V1–V3). In the scanner, participants (5 female, 3 male) were cued to covertly attend to one of two spatially competing letter streams, each defined by low or high SF content. This task promoted feature-based attention directed to a particular SF, as well as the suppression of the irrelevant stream's SF. Concurrently, we measured pSFT in a task-irrelevant hemifield to examine how the known spatial spread of feature-based attention influenced the SF tuning properties of neurons sampled within a voxel. We discovered that attention elicited attractive shifts in SF preference, towards the attended SF. This suggests that attention can profoundly influence populations of SF preference across the visual field, depending on task goals and native neural preferences.

Significance Statement

The spatial frequency (SF) preference of neural populations in early visual cortex governs the coarse and fine details we can see. However, the brain is limited in what it can process, requiring selective attention to prioritize relevant over irrelevant details. Although SF is fundamental to visual processing, it remains unclear how selective attention to SF alters population-level responses to SF. Using fMRI, we measured SF preferences in V1–V3 while participants deployed feature-based attention to one of two competing stimuli solely defined by their SF. We found that attention produced attractive shifts in preferences across the visual field, towards the attended

SF, demonstrating that voluntary attention can flexibly reshape SF preferences in early visual cortex.

Introduction

Signals in our brain are constantly vying for metabolic resources (Lennie, 2003), imposing a limit on the content and fidelity of information available for processing from moment to moment (Simoncelli and Olshausen, 2001; Carandini et al., 2005). Attention is theorized to play a key role in selectively regulating competing representations, prioritizing the processing of behaviorally relevant features, while suppressing the irrelevant (Lee et al., 1999; Carrasco, 2011; Maunsell, 2015; Wu, 2024). Indeed, attention has been known to boost the gain of populations that represent attended items (Carrasco, 2011; Maunsell, 2015; Maunsell and Treue, 2006; Ling et al., 2015; Liu, 2019), an effect that has been reported neurally in animals (Treue and Maunsell, 1996; Treue and Martínez-Trujillo, 1999; Martinez-Trujillo and Treue, 2004; David et al., 2008; Zhang and Luck, 2009; Cohen and Maunsell, 2011) and humans (Sasaki et al., 2001; Serences et al., 2009; Pestilli et al., 2011; Klein et al., 2014; Foster and Ling, 2022), as well as psychophysically (Fang and Liu, 2019; Herrmann et al., 2012; Ling et al., 2009). Moreover, these modulatory effects of attention are believed to impinge upon a cornerstone selective property in early vision: spatial frequency processing (David et al., 2008; Carrasco et al., 2006). The spatial frequencies a neural population selectively responds to is synonymous with the density of spatial detail it can encode (Blakemore and Campbell, 1969; Braddick, 1981; De Valois et al., 1982). Therefore, given the critical role of this selectivity in governing what we can and cannot see at any given moment, the ability to augment it would grant attention significant power to shape perception (Anton-Erxleben and Carrasco, 2013). However, while SF is implicated as a modulatory target for resolving competition between representations (Sowden and Schyns, 2006; Anton-Erxleben and Carrasco, 2013), there is a gap in our understanding of how attention modulates population responses to SF to resolve competition, particularly in human cortex (Pouget et al., 2000; Jazayeri and Movshon, 2006; Sowden and Schyns, 2006; Fang and Liu, 2019).

To bridge this gap, we leveraged a model-based fMRI technique, population spatial frequency tuning (pSFT), which can efficiently estimate both the preferred SF (pSFT peak) and the range of SFs that elicit a response (pSFT bandwidth) in neural subpopulations sampled within a voxel (Aghajari et al., 2020). We paired this technique with a novel feature-based attention paradigm, in which participants selectively attended one of two streams of letters, defined by their distinct SF properties. In doing so, we were able to assess voxel-wise changes in SF processing within and across early visual cortices (V1–V3). Our results revealed profound shifts in the peak SF preference and bandwidth of subpopulations throughout early visual cortex that depended on the nature of the attentional task and stimuli. Specifically, we discovered that attention elicited substantial *attractive shifts* in SF preference towards the attended SF: subpopulations that innately preferred SFs lower than the attended item shifted higher, and those that innately preferred higher SFs shifted lower. Evidently, feature-based attention has the power to flexibly alter SF tuning for individual subpopulations, shifting cortical SF preferences to dynamically process the qualities of attended items.

Materials and Methods

Subjects. Eight healthy adult volunteers (5 female) between ages 22 and 33 (age = 27.3 ± 1.6, mean ± standard error of the mean, SEM) participated in the experiment. All subjects had normal or corrected-to-normal vision. This sample size was chosen to mirror the original population spatial frequency tuning mapping study by Aghajari, Vinke, & Ling (Aghajari et al., 2020). All subjects involved provided written consent and were reimbursed for their time. The Boston University Institutional Review Board approved the study.

Apparatus and Stimuli. In the testing room used for initial calibration and training, stimuli were displayed on a gamma-corrected Display++ LCD monitor (Cambridge Research Ltd, resolution: 1440 x 1080 pixels, refresh rate: 100 Hz; viewing distance: ~114 cm, the distance needed to

mimic the pixels per degree in the scanner setup), with no additional light sources in the room. Participants were seated with their chin on a padded chin rest and forehead rested.

In the MRI scanner bore, stimuli were displayed on a linearized, gamma-corrected rear-projected screen (VPixx PROPixx DLP LED; resolution: 1024 x 768-pixels; refresh rate: 60 Hz; viewing distance: ~99 cm), with no additional light sources in the room. All stimuli were presented on a uniform gray background (mean luminance: ~150 cd/m^2). A dot was presented at the center of the display for fixation (diameter: 0.15 degrees of visual angle, °). Stimuli were generated using MATLAB 2017b (The MathWorks Inc., 2017) and the Psychophysics Toolbox (Brainard, 1997) rendered on Ubuntu 18.04.3 LTS.

The visual display was partitioned into attended (task-relevant) and unattended (task-irrelevant) hemifields during task blocks. At the attended hemifield, two rapidly updating letter streams were superimposed (4 Hz character refresh rate; eccentricity = 3.5° horizontal from fixation; diameter = 3°). Each letter stream contained spatial frequency bandpass-filtered Sloan letters, with a center SF of 0.5 cpd and 2 cpd, respectively (filter width: 0.2; gaussian smoothing kernel width: 3). Letter characters consisted of A, C, D, J, K, L, M, P, S, V, X, Y, and Z. Letter characters did not repeat sequentially within a letter stream nor was the same letter presented simultaneously between letter streams. Target letters J and K had a 20% probability of occurrence. To avoid the effects of attentional blink (Dux and Marois, 2009), there was at least 500 ms between target letters within a letter stream.

At the unattended visual hemifield, a pseudorandom sequence of 40 SF-bandlimited noise stimuli were presented (10 Hz noise sample refresh rate), with center SFs that were logarithmically spaced from 0.1 cpd to 12 cpd (filter width: 0.2). These stimuli were presented at 100% Michelson contrast and through a wedge aperture that subtended 5° from fixation (outer radius: 9.18°; inner radius: 0.32°). At center fixation, the dot changed from white to black between rest periods and task blocks. During task blocks, the dot would pseudorandomly change in luminance from 0 to 30, with the same target probability as the target letters. Stimulus presentation statistics were identical in every block.

Five subjects (S1, 2, 3, 4, and 7) had the probe stimuli on the left visual hemifield (pSFT analyzed from the right hemisphere), while the remaining subjects (S5, 6, and 8) had the probe stimuli on the right visual hemifield (pSFT analyzed from the left hemisphere). Results did not significantly differ when data were grouped and compared by probe hemisphere (Wilcoxon ranked sum test $p > 0.05$).

Spatial frequency-bandpass filtering. All stimuli were SF-bandpass filtered in MATLAB 2017b scripts. The Sloan letters used (Pelli et al., 1988) were imported as TIFF files and resized so that the diameter of the letters spanned 3°. To resize the images appropriately, we calculated a pixel-based ratio between the letter size and image size to determine how much the image width needed to be resized to achieve the desired letter diameter. Next, the complement of each letter image was taken, reversing the luminance of each pixel so that the background changed from white to black and the letters from black to white. The *fft2* MATLAB function was used to apply a 2D fast Fourier transform (FFT) on the image, followed by *fftshift* to shift the DC component to the center of the frequency domain.

A 2D bandpass filter (σ = 0.2) was generated with the *Bandpass2* function from *Psychtoolbox*. The filter matched the size of the image, and the radial cut-off frequencies, fLow and fHigh, were divided by the Nyquist frequency, $f_{Nyquist} = 1/(2 * pixel\ size\ (cm))$ to create a circularly symmetric filter. The 2D bandpass filter was smoothened with the *imgaussfilt* function with a standard deviation of 3 pixels for the letter images and a tenth of the pixels per degree of visual angle for the noise stimuli. The filter was normalized by subtracting the minimum value from each element then dividing the difference by the range. Next, the normalized bandpass filter was applied to the shifted FFT image. To inverse the FFT and return the image to the spatial domain, the *ifftshift* and *ifft2* functions were applied to the image, in that order.

To finalize the images, the minimum value was subtracted from each element then the difference was divided by the range in the case of letter stimuli, or by the maximum in the case of the noise stimuli. Finally, the filtered images were rectified (taking the absolute value) and

converted to a visible range of pixel values between 0 to 255 for drawing by scaling every element by 127 then adding 127.

Eye tracking. An MRI-compatible EyeLink 1000 Plus infrared eye tracker (SR Research) was used to monitor gaze position and pupil size throughout the experiment at a sampling rate of 500 Hz. Each scan began with eye calibration and validation. Subjects were instructed to maintain fixation throughout the study. Eye data were analyzed with custom MATLAB scripts. Average pupil size, horizontal gaze position, and fixation stability (quantified as the bivariate contour ellipse area (Crossland et al., 2004)) were compared with a 1-way ANOVA to confirm no significant differences between conditions at the group level.

Main Task. Each task run consisted of an initial 10-s blank period and six 40.5-s task blocks, each followed by a 10-s blank period (313 TRs per run). Before a task block, participants were briefly presented one of three color cues at fixation (1-s duration), indicating which task to perform: a low SF letter detection task at 0.5 cpd (*Attend LSF* condition), a high SF letter detection task at 2 cpd (*Attend HSF* condition), or a luminance change detection task at fixation (*Attend Fixation* condition). The task block began 30 ms after cue offset. The fixation dot was black during task blocks and white during blank periods. Color cues were randomly assigned per subject, and task conditions were randomly interleaved, with 2 blocks per condition in each task scan (9 task scans per subject; 18 blocks per condition per subject).

In the *Attend Fixation* condition, subjects reported with a button press the detection of a brief (250-ms) change in luminance, from black to gray (0 to 30), at central fixation. In the letter detection task (*Attend LSF* and *Attend HSF* conditions), participants were cued to covertly attend to one of two superimposed letter streams and report the detection of a target letter J or K by pressing the left or right button, respectively (response window = 1 s).

Before scanning, participants completed a 1-hour stimulus calibration and training session. Calibration involved participants maintaining fixation while adjusting the alpha level of the LSF letter stream, which began at an alpha level of 127 by default (where 0 = complete transparency and 255 = complete opacity). Participants could adjust the size of the increments if needed. Participants were instructed to reach an alpha level that allowed for comparable

197 detection of the target letters between letter streams, with emphasis made on achieving an alpha
198 level where neither letter stream appeared to dominate the other.
199 When participants found a satisfactory alpha level for the LSF letter stream, the new
200 alpha level was applied to training. Training involved performing at least 3 runs of the main task
201 (at least 6 blocks per condition in total). If the difference in performance between conditions was
202 greater than 10%, participants either completed additional training runs or could readjust the
203 alpha level of the LSF letter stream. Either case was followed by additional training until the
204 difference in performance between *Attend LSF* and *Attend HSF* conditions was roughly 5-10% or
205 time constraints were met.
206 Outside the scanner bore and on scan-day, subjects practiced the task on a Lenovo
207 ThinkPad laptop to reconfirm performance was comparable (3 runs maximum so that we had
208 enough time to complete all 9 scan runs of the main task). In the scanner bore and before the
209 main task, subjects had an opportunity to adjust the LSF letter stream alpha level (mean alpha
210 level = 168, SD = 31.3). After confirming the alpha level, participants completed anatomical
211 scans, two probe localizer scans, and nine main task scans. The localizer scans were not used in
212 final analyses due to the letter stream spatial localizer being kept at 2.5° eccentricity (the settings
213 from a pilot study) instead of the 3.5° eccentricity used in the main experiment. Behavioral
214 performance in the main experiment was measured as percent correct and analyzed with a 1-way
215 ANOVA to confirm no significant differences in performance between conditions at the group
216 level.
217 **Functional magnetic resonance imaging data acquisition.** All high-resolution brain data was
218 collected at the Boston University Cognitive Neuroimaging Center, which houses a Siemens 3T
219 Prisma scanner equipped with a 64-channel head coil provided by Siemens Healthcare. A whole-
220 brain anatomical scan was acquired with a T1-weighted multi-echo Magnetization Prepared
221 Rapid Gradient Echo (MPRAGE) sequence (1.2 mm^3; FOV = 192 $\times$ 192 $\times$ 176 mm; fractional
222 anisotropy flip angle (FA) = 7°; TR = 2200 ms; TE = 1.57 ms; TI = 1100 ms) (Van Der Kouwe et
223 al., 2008). All BOLD data for the main task were acquired with a T2*-weighted in-plane Echo
224 Planar Imaging (EPI) pulse sequence with simultaneous multi-slice (SMS) imaging and a field of

view perpendicular to the calcarine sulcus (2 mm^3 voxels; FOV = 936 × 936 × 313 mm (Probe Localizer FOV = 936 × 936 × 320 mm); FA = 64°; TR = 1000 ms; TE = 30 ms) (Moeller et al., 2010; Xu et al., 2013). BOLD data for the pRF mapping session was acquired with a T2*-weighted in-plane EPI-SMS imaging sequence and a FOV perpendicular to the calcarine sulcus, but with the following parameters: 2 mm^3 voxels; FOV = 60 × 112 × 172 mm; FA = 80°; TR = 1000 ms; TE = 35 ms. We used the University of Minnesota's CMRR-MB pulse sequence for SMS-EPI acquisition.

Anatomical analysis. Whole-brain T1-weighted anatomical data was processed through the 'recon-all' pipeline provided by the FreeSurfer neuroimaging analysis software (Fischl, 2012). The output was a model of the cortical surface that allowed for surface-based registration between functional and structural MRI data, ensuring that pRF and pSFT data were accurately mapped to the 3D space defined by the functional MRI volumes.

Functional magnetic resonance imaging data pre-processing. All functional BOLD time series data were corrected for EPI distortions with a reverse phase-encoded method via the Functional MRI of the Brain Software Library (FMRIB) (Andersson et al., 2003). All fMRI fieldmap-corrected data were preprocessed with FreeSurfer Functional Analysis Stream (FS-FAST) (Fischl, 2012), which applied standard motion correction procedures, Siemens slice timing correction, and boundary-based registration between functional and anatomical 3D spaces (Greve and Fischl, 2009). To allow for voxel-wise analysis of the data, no volumetric spatial smoothening was applied (FWHM = 0). Moreover, accurate volumetric alignment of functional data between scan runs was attained by applying robust rigid registration (Reuter et al., 2010). The target volume for alignment was designated as the middle time point of the first run from each session, while the middle time point of subsequent runs was used as the moveable volume for alignment.

Population receptive field mapping. Every participant completed an independent population receptive field (pRF) mapping session. The pRF analysis was used to manually create ROI labels for early visual areas V1, V2, and V3. Each session involved 3–5 scans of both (A) rotating

wedge stimuli, and (B) bar sweep and expanding/contracting ring stimuli. All stimuli were presented on a mean luminance background and consisted of colored objects and faces of varying sizes over a pink noise background. During stimulus presentation, participants performed a color change detection task at fixation, pressing a button when the fixation dot changed from red to white or white to red. The data acquired from these scans were analyzed with the *analyzePRF* toolbox for MATLAB (Kay et al., 2013), which estimates the visual field eccentricity, polar angle, and receptive field size for every voxel within the cortical ribbon of the occipital lobe.

Population spatial frequency tuning mapping. Estimating population spatial frequency tuning (pSFT) from fMRI BOLD signals was contingent on the assumption that the BOLD signal is a product of a linear system (Boynton et al., 1996), an assumption often made in generating population receptive fields with fMRI (Dumoulin and Wandell, 2008). Additionally, due to the 10-s blank period in between blocks, we could concatenate voxel time-series across every scan with respect to condition (*Attend LSF*, *Attend HSF*, or *Attend Fixation*), resulting in 18 spliced time-series blocks per condition. Altogether, three sets of SF input and measured BOLD time series were fed into the pSFT model fitting pipeline (Figure 1C).

We assumed that BOLD responses to spatial frequencies, $R(f)$, can be characterized by a log-Gaussian distribution (Aghajari et al., 2020) (Eq. 1), expressed as:

$$R([f(t)]) = e^{-\frac{[\log(f(t)) - \log(\mu)]^2}{2\,\sigma^2}} \quad (1),$$

where $f(t)$ is the SF presented at time t, μ is the SF that produces the maximum response of the population (the "pSFT peak"), and σ is the linear SF tuning bandwidth — μ and σ being unknown. Because SF mapping stimuli were not presented during the blank periods in between blocks, the SF input during the blank periods was set to 0.0001 to avoid taking the log-transform of 0.

The population response, $R[f(t)]$, was then convolved with a hemodynamic impulse response function, $h(t)$, to generate a predicted BOLD signal, $B(t)$:

$$B(t) = \beta_0 + \beta \cdot R[f(t)] * h(t) \quad (2),$$

where β_0 and β are unknown and represent the baseline and a scaling coefficient for the BOLD percent signal change, respectively. The hemodynamic impulse response function (HIRF), $h(t)$, was a gamma function of the form:

$$h(t) = \frac{(t/\tau)^{(n-1)} e^{-(t/\tau)}}{\tau(n-1)!} \quad (3),$$

where τ is the time constant (fixed to a value of 1.08), n is the phase delay (fixed to a value of 3), and t the delay between stimulus onset and the BOLD response (fixed to a value of 2.05) (Boynton et al., 1996). We performed non-linear regression to search for the most optimal μ, σ, β, and β_0 values, with the objective of minimizing the sum-of-squares error (SSE) between the predicted and measured BOLD percent signal change (via the *fmincon* function in MATLAB). Based on parameter bounds used in Aghajari, Vinke & Ling 2020 (Aghajari et al., 2020), we constrained μ to values between 0.009 and 6, σ to values between 0.1 and 4, β_0 to values between -10 and 10, and β to values between -25 and 25.

To identify optimal starting values for non-linear regression, we performed a preliminary coarse-to-fine grid search of model parameters. With the parameter constraints defined above, the coarse grid search contained a combination of 10 logarithmically-spaced μ values and 10 linearly-spaced σ values, while β and β_0 were fixed to 1 and 0 respectively. The combination of values that produced the lowest SSE in the coarse-grid search were then used to generate a range of μ and σ values for the fine-grid search. Specifically, in the fine grid search, 100 logarithmically-spaced values for μ and 100 linearly-spaced points for σ were generated between half and double the optimal coarse-grid search result for each parameter. β and β_0 were again fixed to 1 and 0, respectively. The combination of values that produced the lowest SSE in the fine grid search were then used as the initial μ, σ, β, and β_0 values for non-linear regression. If multiple values produced the minimum SSE, their average was used.

Voxel selection. In each ROI, which were defined by the results of the pRF mapping procedure, we selected voxels whose pRF eccentricity were within 0.16–9.8°, pRF sizes greater than 0.1° in diameter, polar angle within the probe aperture (if on the left hemifield: 100° < θ < 260°; if on the right hemifield: 280° < θ < 80°), and pRF R^2 greater than 10%. All reported effects on pSFT are

contingent on this independent pRF analysis and thus avoid circular data selection errors (Stoll et al., 2022). As an additional voxel criterion for analysis inclusion, we selected voxels with pSFT R^2 greater than 10%, μ estimates between 0.01 and 5 cpd, and linear SF tuning bandwidth σ between 0.10 and 4 cpd. Lastly, we excluded voxels whose μ or σ estimates were three standard deviations away from the mean in any ROI and attention condition. These criteria left 100 ± 18 (50) (mean ± SEM (SD)) voxels in V1 [20 ± 2 (6)% remaining], 92 ± 12 (35) in V2 [19 ± 1 (5) % remaining], and 50 ± 6 (16) voxels in V3 [14 ± 1 (4)% remaining], which is comparable to previous counts (Vo et al., 2017; Foster and Ling, 2022) given that pSFT estimates were acquired in only one visual hemisphere.

Attentional modulation index. To quantify changes in pSFT with attention, we computed voxel-wise attentional modulation indices (AMI) for pSFT peak and pSFT bandwidth. Calculating AMI involved taking the difference in parameter estimates between conditions and dividing this difference by their sum (Van Es et al., 2018; Treue and Maunsell, 1996; Gandhi et al., 1999; Cohen and Maunsell, 2011; Ni and Maunsell, 2019), followed by a percentage conversion:

$$AMI\ (\%) = \frac{A-B}{A+B} \times 100 \quad (4)$$

Dissimilarity from attended spatial frequency. To test for preference-dependent changes in pSFT with attention, we computed a voxel-wise dissimilarity metric between the baseline pSFT peak and the attended SF:

$$\text{Dissimilarity from LSF (octaves)} = \log_2[\frac{\mu_{baseline}}{0.5}]$$

$$\text{Dissimilarity from HSF (octaves)} = \log_2[\frac{\mu_{baseline}}{2.0}].$$

For example, voxels an octave above the attended LSF have a pSFT peak of 1 cpd in this space, while those same voxels would be an octave below the attended HSF.

Line fitting. To test whether attentional modulation of pSFT is preference-dependent, we calculated subject-wise linear slopes between dissimilarity from the attended SF versus pSFT AMI, pRF eccentricity versus pSFT AMI, and pRF size versus pSFT AMI. The MATLAB function *polyfit* was used to find coefficients of a first-degree polynomial, fitting AMI best in a least-squares sense across voxels within an ROI and condition for each subject.

Statistical analyses. All statistical analyses were performed in MATLAB. Subject averages were assumed to be normally distributed. To test for differences in task performance, pupil size, gaze position, gaze stability, and pSFT estimates between conditions, 1-way ANOVA were performed at the group level. One-sample t-tests and paired-sample t-tests were performed on values that were computed relative to the baseline condition (e.g., attentional modulation indices and slopes from the *Attend LSF* and *Attend HSF* conditions). Effect sizes (Cohen's d) were calculated using the one- and paired-sample(s) formula to compare AMI within and between *Attend LSF* and *Attend HSF* conditions. To estimate 95% confidence intervals, we used bootstrap resampling (1,000 iterations), where data was sampled with replacement and Cohen's d was recomputed every iteration. The 2.5% and 97.5% percentiles of the bootstrapped distribution defined the confidence bounds. With n = 8, α = 0.05, and 80% power, we can reliably detect an effect size of ±1.16. Repeated measures correlation coefficients and p-values were calculated to test the relationship between change in peak and change in bandwidth (Bakdash and Marusich, 2017). Single, double, and triple asterisk correspond to Bonferroni-corrected p-values of 0.05, 0.01, and 0.001 to account for the possibility of type-I error in one-sample t-tests and paired-sample t-tests.

Code Accessibility. Code used for the experiment and data analyses can be found on the Open Science Framework at https://osf.io/meq9n/?view_only=e3b6a5af43514e2795d6243468db8a4c.

Results

In an MRI scanner, participants performed one of three tasks in a blocked design (Figure 1A): a low SF letter detection task at 0.5 cycles per degree (cpd) (*Attend LSF* condition), a high SF letter detection task at 2 cpd (*Attend HSF* condition), and a luminance change detection task at fixation (*Attend Fixation* condition). The *Attend LSF* and *Attend HSF* conditions involved covertly attending to one of two superimposed letter streams (left hemifield of the example display in Figure 1B) and reporting the detection of target letters J and K with a left and right button press, respectively. This spatial co-localization of the letters was designed to induce sufficient competition between the low and high SF letter streams, with the assumption that attending to a specific letter stream would promote attention to a specific band of SF content (Lee et al., 1999;

White et al., 2015). Because SFs are processed by distinct sub-populations (Blakemore and Campbell, 1969; Ware and Mitchell, 1974), we hypothesized that selective attention to a low and high SF targets distinct sub-populations across the visual field (Maunsell and Treue, 2006; Fang and Liu, 2019; Liu, 2019). These sub-populations are then read as a shift in peak SF and/or change in bandwidth when responses are measured across them (Ling et al., 2015).

To test this hypothesis, we measured and compared condition-specific voxel-wise pSFT in the task-irrelevant hemifield, where participants concurrently and passively viewed a range of bandlimited noise stimuli (right hemifield of the example display in Figure 1B). This design exploits the well-established finding that the modulatory effects of feature-based attention *spread across the visual field* (Saenz et al., 2002), allowing us to interrogate changes in SF processing in a spatially unattended hemifield. Moreover, display statistics were identical in every block and separated by a 10-second blank period, allowing us to concatenate BOLD time series data with respect to a condition (Figure 1C). Before evaluating the influence of attention on pSFT, we confirmed that in every condition pSFT peak decreased and pSFT bandwidth increased with pRF eccentricity and visual area (Figure 1D) (Sasaki et al., 2001; Henriksson et al., 2008; Aghajari et al., 2020; Broderick et al., 2022). Additionally, because the covertly attended location was identical between *Attend LSF* and *Attend HSF* conditions, and no significant differences in task performance, pupil size, gaze position, nor gaze stability were found between conditions at the group level (Figure S1B–C), we could attribute any differences in pSFT between the *Attend LSF* and *Attend HSF* conditions to feature-based attention.

Attentional modulation of pSFT

To quantify changes in pSFT due to attention, we computed voxel-wise attentional modulation indices (AMI) for pSFT peak and bandwidth. Calculating AMI involved taking the difference in parameter estimates between conditions, dividing the difference by their sum, then converting the value to a percentage. By normalizing the difference in pSFT estimates between conditions by their total magnitude, this AMI measure emphasizes relative changes (Cohen and Maunsell, 2011; Treue and Maunsell, 1996; Gandhi et al., 1999; Van Es et al., 2018; Ni and

Maunsell, 2019). Here, changes in peak and bandwidth due to attending the LSF or HSF were calculated relative to the *Attend Fixation* condition, which served as our baseline (Figure 2A). If attentional modulation of pSFT in the task-irrelevant hemifield is evident and dependent on the attended SF, then we expected that the change in peak and/or bandwidth would significantly differ between *Attend LSF* and *Attend HSF* conditions.

Indeed, we found significant differences in the change in peak between *Attend LSF* and *Attend HSF* conditions at the group level (V1, V2 *ps* < 0.05, V3 $p < 0.01$; Cohen's d: V1 = -1.29 [-3.64, -0.65], V2 = -1.29 [-2.47, -0.92], V3 = -1.80 [-6.35, -1.17]; Table 1). Generally, attending the LSF decreased the pSFT peak (Cohen's d: V1 = -0.38 [-1.89, 0.28], V2 = -0.73 [-2.40, -0.27], V3 = -0.53 [-1.31, 0.13]), while attending the HSF increased the pSFT peak (Cohen's d: V1 = 0.20 [-0.93, 0.80], V2 = 0.41 [-0.27, 1.26], V3 = 0.51 [-0.12, 1.68]). In tandem, attending the LSF decreased the range of SFs that elicited a response (i.e., sharper tuning bandwidth; Cohen's d: V1 = -0.64 [-1.73, 0.03], V2 = -0.28 [-1.09, 0.46], V3 = -0.12 [-0.82, 0.87]), and attending the HSF even more so (Cohen's d: V1 = -1.05 [-2.25, -0.52], V2 = -0.95 [-2.44, -0.39], V3 = -0.72 [-1.72, -0.17]). Though, there were no significant differences in the change in bandwidth between conditions (*ps* > 0.05; Cohen's d: V1 = 0.97 [0.40, 2.37], V2 = 0.93 [0.32, 2.43], V3 = 0.82 [0.42, 1.78]; Table 1). Lastly, in V1, we found a significant decrease in BOLD amplitude in both *Attend LSF* and *Attend HSF* conditions (*ps* < 0.05), in agreement with the expected effects of covert spatial attention on the BOLD response of unattended locations (Gouws et al., 2014). We also found an increase in baseline in V1 in the *Attend HSF* condition ($p < 0.05$; Table S1). Altogether, this suggests that feature-based attention to SF elicited global attractive shifts in preferred SF and increased selectivity.

Interestingly, upon closer inspection, we found a range of modulation strategies in every visual area.

To elaborate, a change in pSFT for an individual voxel can fall under four strategies that consist of combinations of whether lower or higher SFs are prioritized (change in peak) and whether bandwidth is broadened or sharpened (change in bandwidth) (Figure 2B). When correlated against one another, what is the dominant relationship between changes in peak SF

and bandwidth? In every visual area we found a moderate negative correlation between attentional modulation of peak and bandwidth in both *Attend LSF* and *Attend HSF* conditions (*ps* < 0.001). In other words, a decrease in peak SF was associated with an increase in bandwidth, while an increase in peak SF was associated with a decrease in bandwidth (Figure 2C).

Because the observed changes in pSFT were consistent across early visual cortex, we wondered whether changes in tuning with feature-based attention to SF were driven by a feature-similarity mechanism (Maunsell and Treue, 2006; Liu, 2019), wherein sub-populations most similarly tuned to the attended feature experience increased response gain (Treue and Martínez-Trujillo, 1999; Martinez-Trujillo and Treue, 2004; Maunsell and Treue, 2006; Ling et al., 2009; Fang and Liu, 2019). We reasoned that if attentional modulation of pSFT were dependent on the dissimilarity between the baseline peak SF and the attended SF, then the rate of change in pSFT as a function of dissimilarity should significantly differ from zero.

To test for similarity-dependent modulation of pSFT, we first computed a voxel-wise dissimilarity metric between the baseline pSFT peak and attended SF (dissimilarity from the attended SF (octaves) = $\log_2[\mu_{baseline}/attended\ SF]$). We then assessed subject-wise linear slopes between the baseline dissimilarity and change in peak and bandwidth in every visual area and condition. The sign of the slope—positive or negative—would indicate a repulsive or attractive effect for changes in peak SF, respectively. Similarly, for changes in bandwidth, positive or negative slopes would correspond to sharper-to-broader or broader-to-sharper bandwidths with increasing dissimilarity.

From V1 to V3, we found negative slopes for the change in peak as a function of baseline dissimilarity (Figure 3A*,* Figure 4A). More specifically, feature-based attention appeared to cause attractive shifts in peak SF when attention was directed to the lower SF (V1, V3 *ps* < 0.05), and even stronger shifts when directed to the higher SF (V1, V3 *ps* < 0.01). In V1 and V3, we found significant differences in the magnitude of attractive shifts between *Attend LSF* and *Attend HSF* conditions (*ps* < 0.05). While visual inspection suggests otherwise, we found no significant attractive shifts in peak SF in V2 within conditions nor between them (Figure 4A and Table 2). In tandem, there was a positive relationship between baseline dissimilarity and change in bandwidth

(Figure 3B, Figure 4B). This “sharper-to-broader” relationship across the preference space was significant only in V1 and V2 when attending the LSF (*ps* < 0.01; Table 1).

Attentional modulation of pSFT as a function of pRF

The spatial resolution hypothesis posits that attention resolves differences in spatial sampling (i.e., resolution) between foveal and peripheral populations (Yeshurun and Carrasco, 1998; Anton-Erxleben and Carrasco, 2013; Barbot and Carrasco, 2017). Although we could not measure changes in pRF with our experimental design, nor changes in pSFT in the attended hemifield, we wondered if there was a relationship between the baseline pRF (eccentricity and size; Figure S3) and changes in pSFT (Text S1), as SF preferences vary systematically with eccentricity and correlate with size (Aghajari et al., 2020; Broderick et al., 2022; Henriksson et al., 2008; Yu et al., 2010; Kirsch and Kunde, 2023). Only in V3 and the *Attend HSF* condition did we find a significantly positive linear relationship between pRF eccentricity and change in peak (p < 0.01; Figure S2A, Table S2). Additionally, we found a significantly positive relationship between pRF size and change in peak in both conditions in V3 (*Attend LSF*, p < 0.05; *Attend HSF*, p < 0.001; Figure S2B, Table S3). Lastly, we found significant differences in the rate of change in pSFT peak as a function of pRF size and eccentricity *between* conditions in V3 (*ps* < 0.05), altogether supporting the possibility that selective attention to the LSF and HSF triggered unique changes in spatial resolution.

Discussion

The existence of SF selective neurons in the early human visual system provides a window into how spatial patterns across the visual field are processed (Braddick, 1981). SF processing in human visual cortex can be characterized as a set of parallel but interconnected narrow-band “channels” that together enable the perception of a wide range of spatial details across the retinal image (Wilson and Wilkinson, 1997; Kauffmann et al., 2014). If we assume that the convergence of neural populations across the early visual system are the constituents of these channels, then attention to SF should steer the center and/or width of SF-tuned responses

towards the attended SF across the visuocortical hierarchy, as proposed in past research but not yet confirmed in humans (Schyns, 1998; Sowden and Schyns, 2006; David et al., 2008). Here, we addressed this gap in knowledge by acquiring pSFT in early visual cortex (V1–V3) while manipulating selective attention to SF. We discovered profound shifts in tuning preferences for voxels in early visual cortex, towards the SF content of an attended item. Below, we contextualize our findings and explore potential explanations for the observed changes in pSFT with attention.

In our task, participants were instructed to detect target letters in one of two superimposed letter streams that were low- and high-pass filtered, respectively. In both the *Attend LSF* and *Attend HSF* condition, one could argue that texture segmentation at the covertly attended location is required to separate the relevant from irrelevant SF content (Yeshurun and Carrasco, 2000). Relative to a baseline condition where the letters were ignored, we found that feature-based attention triggered significantly distinct attractive shifts in SF preference, towards the attended SF and across early visual field maps of the unattended hemifield, along with increased selectivity for the newly preferred SF. From V1–V3, LSF-preferring populations experienced the greatest increase in pSFT peak and decrease in bandwidth, while more HSF-preferring populations experienced the greatest decrease in pSFT peak and increase in bandwidth (Figures 3 and 4). Together, this demonstrates that changes in pSFT with attention are likely dependent on both the native SF tuning being sampled and the attended SF.

More specifically, we believe our findings are the consequence of covert spatial attention and feature-based attention selectively targeting neural subpopulations across the visual field (Saenz et al., 2002; White et al., 2015) to trigger attractive shifts along the task-relevant feature domain (Saenz et al., 2002; Womelsdorf et al., 2006; David et al., 2008; Klein et al., 2014; Liu, 2019; Chapman et al., 2023). While the shifts in preferred SF were significantly different between *Attend LSF* and *Attend HSF* conditions, the magnitude of the shifts within conditions were not (though this could be due to insufficient power). This is expected, in part because the SF tuning of a neural population sampled within a cortical column is ultimately constrained by its underlying neural architecture and thus cannot completely change its tuning profile (Blakemore and Campbell, 1969; Salinas and Abbott, 2001; David et al., 2008).

When moving out towards the periphery, the proportion of neurons within a population that are more selective for HSFs decreases (Sasaki et al., 2001; Aghajari et al., 2020; Broderick et al., 2022). This relationship generates testable predictions for how pSFT might change with feature-based attention. In general, feature-based attention is theorized to operate via a feature-similarity gain mechanism, selectively targeting sub-populations tuned to the attended feature (Maunsell and Treue, 2006). Indeed, human psychophysical data from a 2-IFC task suggests that the feature-similarity gain model with asymmetrical surround suppression can characterize the effects of selective attention to SF (Fang and Liu, 2019). In other words, when an observer attends to a SF, feature-based attention should shift the peak SF response across a neural population towards the attended SF. For example, attending a LSF should target neurons tuned to that SF across the visual field. In central vision, LSF-preferring neurons would experience a gain in response, while HSF-preferring neurons are suppressed, together creating a shift towards lower SFs across a population (Ling et al., 2015). In peripheral vision, SF preferences are much lower relative to central vision, so this effect would instead create an observable shift towards higher SFs. While we believe feature-similarity gain is the primary mechanism, we did find a multitude of modulation strategies (Figure 2C), which might be indicative of a mixture of attentional gain and preferential shifts in tuning at the single unit level (David et al., 2008; Ester et al., 2020).

Because SF tuning is tightly correlated with spatial receptive field characteristics (Altan et al., 2025), and both *Attend LSF* and *Attend HSF* conditions required covert spatial attention, our results likely align with the spatial resolution hypothesis, which proposes that covert attention resolves differences in spatial resolution between foveal and peripheral populations (Yeshurun and Carrasco, 1998; Anton-Erxleben and Carrasco, 2013; Barbot and Carrasco, 2017). There are signatures in our results that intersect with the predictions of the spatial resolution hypothesis. First, psychophysical studies that support the spatial resolution hypothesis reason that covert attention improves perception by selectively targeting small, HSF-selective RFs in the periphery (increasing resolution) and LSF-selective RFs in central vision (decreasing resolution) (Yeshurun and Carrasco, 2000; Carrasco et al., 2006). In other words, attention can flexibly adjust spatial

resolution with respect to task demands and native spatial sampling characteristics (Yeshurun and Carrasco, 1998; Yeshurun et al., 2008; Flevaris et al., 2014; Barbot and Carrasco, 2017; Van Es et al., 2018). Indeed, the rate of change in pSFT peak, as a function of the dissimilarity between the baseline pSFT peak and the attended SF, was more negative in the *Attend HSF* condition than in the *Attend LSF* condition in our study, perhaps because the HSF condition requires higher spatial sampling characteristics (i.e., higher pSFT peak and sharper tuning bandwidths) to resolve the high SF letters (Van Es et al., 2018). We also speculate that the observed changes in pSFT here should generalize when the visual system engages in global versus local processing, like in the case of Navon type stimuli (Flevaris et al., 2014).

The flexibility of SF processing might be dependent on the observer's ability to diagnose the most relevant SF (Schyns, 1998), therefore, future studies might investigate the influence of perceptual learning and adaptation on pSFT (Fiorentini and Berardi, 1980; Sowden et al., 2002; Carrasco et al., 2006; Sowden and Schyns, 2006; Altan et al., 2025). The temporal dynamics of attentional modulation of pSFT might be another fruitful avenue of research, as the processing of LSFs and HSFs have unique temporal dynamics (Mazer et al., 2002; Bredfeldt and Ringach, 2002; Purushothaman et al., 2014). There is also a gap in knowledge for whether the covertly attended location and competing SFs at the attended location influence the magnitude of attractive shifts across the visual field (Majaj et al., 2002; Verghese et al., 2012), as physiological evidence has shown that attentional modulation is eccentricity-dependent (Roberts et al., 2007). Future work might leverage this to determine whether selective attention to low/high SF broadens/sharpens pRFs in an eccentricity-dependent manner (Altan et al., 2025). Addressing these questions will further adjudicate the malleability of SF processing with selective attention to SF.

In conclusion, we investigated the impact of selective attention to SF on pSFT in early visual cortex. We found that feature-based attention to a low and high SF triggered unique attractive shifts in pSFT in the unattended hemifield, towards the attended SF. Our results support a dynamic human visual system, with spatial frequency, one of the building blocks of vision, bending to the will of attention.

References

Aghajari S, Vinke LN, Ling S (2020) Population spatial frequency tuning in human early visual cortex. Journal of Neurophysiology 123:773–785.

Altan E, Morgan C, Dakin S, Schwarzkopf DS (2025) Spatial frequency adaptation modulates population receptive field sizes. eLife.

Andersson JLR, Skare S, Ashburner J (2003) How to correct susceptibility distortions in spin-echo echo-planar images: application to diffusion tensor imaging. NeuroImage 20:870–888.

Anton-Erxleben K, Carrasco M (2013) Attentional enhancement of spatial resolution: linking behavioural and neurophysiological evidence. Nat Rev Neurosci 14:188–200.

Bakdash JZ, Marusich LR (2017) Repeated Measures Correlation. Front Psychol 8:456.

Barbot A, Carrasco M (2017) Attention Modifies Spatial Resolution According to Task Demands. Psychol Sci 28:285–296.

Blakemore C, Campbell FW (1969) On the existence of neurones in the human visual system selectively sensitive to the orientation and size of retinal images. The Journal of Physiology 203:237–260.

Boynton GM, Engel SA, Glover GH, Heeger DJ (1996) Linear Systems Analysis of Functional Magnetic Resonance Imaging in Human V1. J Neurosci 16:4207–4221.

Braddick O (1981) Spatial frequency analysis in vision. Nature 291:9–11.

Brainard DH (1997) The Psychophysics Toolbox. Spatial Vision 10:433–436.

Bredfeldt CE, Ringach DL (2002) Dynamics of Spatial Frequency Tuning in Macaque V1. J Neurosci 22:1976–1984.

Broderick WF, Simoncelli EP, Winawer J (2022) Mapping spatial frequency preferences across human primary visual cortex. Journal of Vision 22:3.

Carandini M, Demb JB, Mante V, Tolhurst DJ, Dan Y, Olshausen BA, Gallant JL, Rust NC (2005) Do We Know What the Early Visual System Does? J Neurosci 25:10577–10597.

Carrasco M (2011) Visual attention: The past 25 years. Vision Research 51:1484–1525.

Carrasco M, Loula F, Ho Y-X (2006) How attention enhances spatial resolution: Evidence from selective adaptation to spatial frequency. Perception & Psychophysics 68:1004–1012.

Chapman AF, Chunharas C, Störmer VS (2023) Feature-based attention warps the perception of visual features. Sci Rep 13:6487.

Cohen MR, Maunsell JHR (2011) Using Neuronal Populations to Study the Mechanisms Underlying Spatial and Feature Attention. Neuron 70:1192–1204.

588 Crossland MD, Sims M, Galbraith RF, Rubin GS (2004) Evaluation of a new quantitative
589 technique to assess the number and extent of preferred retinal loci in macular disease.
590 Vision Research 44:1537–1546.

591 David SV, Hayden BY, Mazer JA, Gallant JL (2008) Attention to Stimulus Features Shifts Spectral
592 Tuning of V4 Neurons during Natural Vision. Neuron 59:509–521.

593 De Valois RL, Albrecht DG, Thorell LG (1982) Spatial frequency selectivity of cells in macaque
594 visual cortex. Vision Research 22:545–559.

595 Dumoulin SO, Wandell BA (2008) Population receptive field estimates in human visual cortex.
596 NeuroImage 39:647–660.

597 Dux PE, Marois R (2009) The attentional blink: A review of data and theory. Attention, Perception
598 & Psychophysics 71:1683–1700.

599 Ester EF, Sprague TC, Serences JT (2020) Categorical Biases in Human Occipitoparietal Cortex.
600 J Neurosci 40:917–931.

601 Fang MWH, Liu T (2019) The profile of attentional modulation to visual features. Journal of Vision
602 19:13.

603 Fiorentini A, Berardi N (1980) Perceptual learning specific for orientation and spatial frequency.
604 Nature 287:43–44.

605 Fischl B (2012) FreeSurfer. NeuroImage 62:774–781.

606 Flevaris AV, Martínez A, Hillyard SA (2014) Attending to global versus local stimulus features
607 modulates neural processing of low versus high spatial frequencies: an analysis with
608 event-related brain potentials. Front Psychol 5.

609 Foster JJ, Ling S (2022) Feature-Based Attention Multiplicatively Scales the fMRI-BOLD
610 Contrast-Response Function. J Neurosci 42:6894–6906.

611 Gandhi SP, Heeger DJ, Boynton GM (1999) Spatial attention affects brain activity in human
612 primary visual cortex. Proc Natl Acad Sci USA 96:3314–3319.

613 Gouws AD, Alvarez I, Watson DM, Uesaki M, Rogers J, Morland AB (2014) On the Role of
614 Suppression in Spatial Attention: Evidence from Negative BOLD in Human Subcortical
615 and Cortical Structures. Journal of Neuroscience 34:10347–10360.

616 Greve DN, Fischl B (2009) Accurate and robust brain image alignment using boundary-based
617 registration. NeuroImage 48:63–72.

618 Henriksson L, Nurminen L, Hyvarinen A, Vanni S (2008) Spatial frequency tuning in human
619 retinotopic visual areas. Journal of Vision 8:5–5.

620 Herrmann K, Heeger DJ, Carrasco M (2012) Feature-based attention enhances performance by
621 increasing response gain. Vision Research 74:10–20.

622 Jazayeri M, Movshon JA (2006) Optimal representation of sensory information by neural
623 populations. Nat Neurosci 9:690–696.

Kauffmann L, Ramanoël S, Peyrin C (2014) The neural bases of spatial frequency processing during scene perception. Front Integr Neurosci 8.

Kay K, Winawer J, Mezer A, Wandell BA (2013) Compressive spatial summation in human visual cortex. Journal of Neurophysiology 110:481–494.

Kirsch W, Kunde W (2023) Human perception of spatial frequency varies with stimulus orientation and location in the visual field. Sci Rep 13:17656.

Klein BP, Harvey BM, Dumoulin SO (2014) Attraction of Position Preference by Spatial Attention throughout Human Visual Cortex. Neuron 84:227–237.

Lee DK, Itti L, Koch C, Braun J (1999) Attention activates winner-take-all competition among visual filters. Nat Neurosci 2:375–381.

Lennie P (2003) The Cost of Cortical Computation. Current Biology 13:493–497.

Ling S, Jehee JFM, Pestilli F (2015) A review of the mechanisms by which attentional feedback shapes visual selectivity. Brain Struct Funct 220:1237–1250.

Ling S, Liu T, Carrasco M (2009) How spatial and feature-based attention affect the gain and tuning of population responses. Vision Research 49:1194–1204.

Liu T (2019) Feature-based attention: effects and control. Current Opinion in Psychology 29:187–192.

Majaj NJ, Pelli DG, Kurshan P, Palomares M (2002) The role of spatial frequency channels in letter identification. Vision Research 42:1165–1184.

Martinez-Trujillo JC, Treue S (2004) Feature-Based Attention Increases the Selectivity of Population Responses in Primate Visual Cortex. Current Biology 14:744–751.

Maunsell JHR (2015) Neuronal Mechanisms of Visual Attention. Annu Rev Vis Sci 1:373–391.

Maunsell JHR, Treue S (2006) Feature-based attention in visual cortex. Trends in Neurosciences 29:317–322.

Mazer JA, Vinje WE, McDermott J, Schiller PH, Gallant JL (2002) Spatial frequency and orientation tuning dynamics in area V1. Proc Natl Acad Sci USA 99:1645–1650.

Moeller S, Yacoub E, Olman CA, Auerbach E, Strupp J, Harel N, Uğurbil K (2010) Multiband multislice GE-EPI at 7 tesla, with 16-fold acceleration using partial parallel imaging with application to high spatial and temporal whole-brain fMRI. Magn Reson Med 63:1144–1153.

Ni AM, Maunsell JHR (2019) Neuronal Effects of Spatial and Feature Attention Differ Due to Normalization. J Neurosci 39:5493–5505.

Pelli DG, Robson JG, Wilkins AJ (1988) The design of a new letter chart for measuring contrast sensitivity. Clinical Vision Science 2:187–199.

Pestilli F, Carrasco M, Heeger DJ, Gardner JL (2011) Attentional Enhancement via Selection and Pooling of Early Sensory Responses in Human Visual Cortex. Neuron 72:832–846.

660 Pouget A, Dayan P, Zemel R (2000) Information processing with population codes. Nat Rev
661 Neurosci 1:125–132.

662 Purushothaman G, Chen X, Yampolsky D, Casagrande VA (2014) Neural mechanisms of coarse-
663 to-fine discrimination in the visual cortex. Journal of Neurophysiology 112:2822–2833.

664 Reuter M, Rosas HD, Fischl B (2010) Highly accurate inverse consistent registration: A robust
665 approach. NeuroImage 53:1181–1196.

666 Roberts M, Delicato LS, Herrero J, Gieselmann MA, Thiele A (2007) Attention alters spatial
667 integration in macaque V1 in an eccentricity-dependent manner. Nat Neurosci 10:1483–
668 1491.

669 Saenz M, Buracas GT, Boynton GM (2002) Global effects of feature-based attention in human
670 visual cortex. Nat Neurosci 5:631–632.

671 Salinas E, Abbott LF (2001) Coordinate transformations in the visual system: how to generate
672 gain fields and what to compute with them. In: Progress in Brain Research, pp 175–190.
673 Elsevier.

674 Sasaki Y, Hadjikhani N, Fischl B, Liu AK, Marret S, Dale AM, Tootell RBH (2001) Local and
675 global attention are mapped retinotopically in human occipital cortex. Proc Natl Acad Sci
676 USA 98:2077–2082.

677 Schyns PG (1998) Diagnostic recognition: task constraints, object information, and their
678 interactions. Cognition 67:147–179.

679 Serences J, Saproo S, Scolari M, Ho T, Muftuler L (2009) Estimating the influence of attention on
680 population codes in human visual cortex using voxel-based tuning functions. NeuroImage
681 44:223–231.

682 Simoncelli EP, Olshausen BA (2001) Natural Image Statistics and Neural Representation. Annu
683 Rev Neurosci 24:1193–1216.

684 Sowden PT, Rose D, Davies IRL (2002) Perceptual learning of luminance contrast detection:
685 specific for spatial frequency and retinal location but not orientation. Vision Research
686 42:1249–1258.

687 Sowden PT, Schyns PG (2006) Channel surfing in the visual brain. Trends in Cognitive Sciences
688 10:538–545.

689 Stoll S, Infanti E, De Haas B, Schwarzkopf DS (2022) Pitfalls in post hoc analyses of population
690 receptive field data. NeuroImage 263:119557.

691 The MathWorks Inc. (2017) MATLAB version: 9.3.0.713579 (2017b).

692 Treue S, Martínez-Trujillo JC (1999) Feature-based attention influences motion processing gain
693 in macaque visual cortex. Nature 399:575–579.

694 Treue S, Maunsell JHR (1996) Attentional modulation of visual motion processing in cortical
695 areas MT and MST. Nature 382:539–541.

696 Van Der Kouwe AJW, Benner T, Salat DH, Fischl B (2008) Brain morphometry with multiecho
697 MPRAGE. NeuroImage 40:559–569.

Van Es DM, Theeuwes J, Knapen T (2018) Spatial sampling in human visual cortex is modulated by both spatial and feature-based attention. eLife 7:e36928.

Verghese P, Kim Y-J, Wade AR (2012) Attention Selects Informative Neural Populations in Human V1. J Neurosci 32:16379–16390.

Vo VA, Sprague TC, Serences JT (2017) Spatial Tuning Shifts Increase the Discriminability and Fidelity of Population Codes in Visual Cortex. J Neurosci 37:3386–3401.

Ware C, Mitchell DE (1974) The spatial selectivity of the tilt aftereffect. Vision Research 14:735–737.

White AL, Rolfs M, Carrasco M (2015) Stimulus competition mediates the joint effects of spatial and feature-based attention. Journal of Vision 15:7.

Wilson HR, Wilkinson F (1997) Evolving Concepts of Spatial Channels in Vision: From Independence to Nonlinear Interactions. Perception 26:939–960.

Womelsdorf T, Anton-Erxleben K, Pieper F, Treue S (2006) Dynamic shifts of visual receptive fields in cortical area MT by spatial attention. Nat Neurosci 9:1156–1160.

Wu W (2024) We know what attention is! Trends in Cognitive Sciences 28:304–318.

Xu J, Moeller S, Auerbach EJ, Strupp J, Smith SM, Feinberg DA, Yacoub E, Uğurbil K (2013) Evaluation of slice accelerations using multiband echo planar imaging at 3T. NeuroImage 83:991–1001.

Yeshurun Y, Carrasco M (1998) Attention improves or impairs visual performance by enhancing spatial resolution. Nature 396:72–75.

Yeshurun Y, Carrasco M (2000) The locus of attentional effects in texture segmentation. Nat Neurosci 3:622–627.

Yeshurun Y, Montagna B, Carrasco M (2008) On the flexibility of sustained attention and its effects on a texture segmentation task. Vision Research 48:80–95.

Yu H-H, Verma R, Yang Y, Tibballs HA, Lui LL, Reser DH, Rosa MGP (2010) Spatial and temporal frequency tuning in striate cortex: functional uniformity and specializations related to receptive field eccentricity. European Journal of Neuroscience 31:1043–1062.

Zhang W, Luck SJ (2009) Feature-based attention modulates feedforward visual processing. Nat Neurosci 12:24–25.

Figures, Tables, and Legends

Figure 1. Experimental design and the pSFT model. (A) Within each scan (nine in total), participants completed two blocks of each condition in a pseudorandom order. (B) The visual display was split into an attended hemifield (task-relevant) and a probe hemifield (task-irrelevant). (C) For each voxel, condition-specific measured BOLD response was compared to a synthesized BOLD response (green trace) produced by the best prediction of pSFT parameters. (D) Estimated pSFT peak (top row) and bandwidth (bottom row) follow expected trends in every condition: decreased pSFT peak and increased bandwidth with pRF eccentricity and visual area. Each point represents a voxel that survived selection criteria. Voxels from all subjects are presented. Each subject has a unique shading in the scatter plots. Green represents estimates from the *Attend Fixation* condition, red from the *Attend HSF* condition, and blue from the *Attend LSF* condition. V1: n = 802, V2: n = 735, V3: n = 398. See also Figure S1A and Table S1.

Figure 2. Attentional modulation of pSFT. (A) The key predictions afforded by the pSFT model are an increase/decrease in the pSFT peak and/or pSFT bandwidth. To facilitate the interpretation of attentional modulation of pSFT, the legend in (B) demonstrates the hypothesized modulatory strategies when the change in peak and bandwidth are plotted against one another. To the right are caricatures of each strategy (quadrants I–IV). In (C), each dot represents a voxel's change in peak (x-axis) and bandwidth (y-axis) in the *Attend LSF* condition (blue, top row) and in the *Attend HSF* condition (red, bottom row). Each subject has a unique shading in the scatter plots. Histograms appended to the north and east wall of each plot reveal the distribution of AMI across all voxels in an ROI. Vertical and horizontal arrows above the histograms represent the group mean (n = 8) for change in peak and bandwidth, respectively. A dot at the intersection of these arrows is included for visibility. The repeated measures correlation coefficient and *p*-value are reported in the top right of each scatter plot. At the group level, the change in peak significantly differed between conditions in every ROI (V1, V2 *ps* < 0.05; V3 $p < 0.01$). V1: n = 802, V2: n = 735, V3: n = 398. See also Table 1.

Figure 3. Attentional modulation of pSFT is preference-dependent. Voxel-wise changes in peak (A) and bandwidth (B) are reported as a percentage and as a function of the octave distance (i.e., dissimilarity) between the voxel's baseline pSFT peak and the attended SF (blue, LSF; red, HSF). Each subject has a unique shading in the scatter plots. Dashed lines represent the group mean (n = 8). Bonferroni-corrected *$p < 0.05$, **$p < 0.01$. V1: n = 802, V2: n = 735, V3: n = 398. See also Figure 4 and Table 2.

Figure 4. **Attentional modulation of pSFT is dependent on the attended SF**. (A) Box plot for baseline dissimilarity versus change in peak slopes. (B) Box plot for baseline dissimilarity versus change in bandwidth slopes. Each box depicts, from bottom to top, the minimum, 25th percentile, median, 75th percentile, and maximum slope across participants. Blue represents values from the *Attend LSF* condition, while red represents values from the *Attend HSF* condition. The '+' symbol represents outliers more than 1.5 times the interquartile range. Statistical test results reported above each plot were performed at the group level within conditions (blue/red) and between conditions (black). Bonferroni-corrected p-values. *ns* $p > 0.05$. *$p < 0.05$. **$p < 0.01$. See also Table 2.

Table 1. Group-level results for change in peak and bandwidth (AMI %). Bonferroni-corrected p-values. *$p < 0.05$. **$p < 0.01$.

Attend LSF
Attend HSF
Attend LSF vs. Attend HSF

	Change in peak			Change in bandwidth		
ROI	**Mean ± 1 SEM**	***p***	**95% CI**	**Mean ± 1 SEM**	***p***	**95% CI**
	-5.65 ± 5.22	0.944	-17.99, 6.69	-6.45 ± 3.54	0.334	-14.83, 1.92
V1	2.28 ± 4.13	1.000	-7.50, 12.05	-10.83 ± 3.64	0.062	-19.45, -2.22
	—	0.024*	-13.05, -2.80	—	0.087	0.60, 8.16
	-8.58 ± 4.16	0.234	-18.41, 1.25	-2.44 ± 3.07	1.000	-9.71, 4.82
V2	5.76 ± 4.97	0.853	-5.99, 17.51	-7.96 ± 2.96	0.093	-14.95, -0.97
	—	0.025*	-23.67, -5.02	—	0.101	0.56, 10.47
	-7.21 ± 4.86	0.544	-18.70, 4.28	-1.21 ± 3.56	1.000	-18.30, 1.31
V3	9.54 ± 6.65	0.583	-6.17, 25.26	-8.50 ± 4.15	0.239	-17.31, 1.20
	—	0.004**	-24.54, -8.96	—	0.162	-0.17, 14.73

773 **Table 2.** Group-level results for linear slopes between dissimilarity from attended SF and change

774 in peak and bandwidth (AMI/oct). Bonferroni-corrected p-value *$p < 0.05$. **$p < 0.01$.

Attend LSF
Attend HSF
Attend LSF vs. Attend HSF

	Change in peak			Change in bandwidth		
ROI	**Mean ± 1 SEM**	***p***	**95% CI**	**Mean ± 1 SEM**	***p***	**95% CI**
	-9.27 ± 2.27	0.014*	-14.65, -3.89	3.31 ± 0.68	0.005**	1.71, 4.91
V1	-10.89 ± 2.46	0.009**	-16.70, -5.08	2.53 ± 1.18	0.211	-0.27, 5.33
	—	0.041*	0.44, 2.79	—	1.000	-2.02, 3.58
	-6.62 ± 2.15	0.053	-11.71, -1.54	3.13 ± 0.69	0.008**	1.50, 4.76
V2	-7.81 ± 2.84	0.085	-14.51, -1.10	2.21 ± 1.84	0.810	-2.15, 6.56
	—	1.000	-4.05, 6.43	—	1.000	-2.91, 4.76
	-7.76 ± 1.94	0.016*	-12.34, -3.17	2.75 ± 1.03	0.097	0.31, 5.19
V3	-12.86 ± 2.14	0.002**	-17.91, -7.81	3.70 ± 1.26	0.065	0.73, 6.67
	—	0.028*	1.71, 8.5	—	0.784	-2.79, 0.89

775

Supplemental Figure and Table Legends

Figure S1. pSFT model performance, behavioral performance, and pupillometry. (A) Box plots for super subject level (i.e., across all voxels) (left panel) and group level (right panel) R^2. Each box depicts, from bottom to top, the minimum, 25th percentile, median, 75th percentile, and maximum R^2. For each ROI, blue (left) represents values from the *Attend LSF* condition, red (middle) from the *Attend HSF* condition, and green (right) *Attend Fixation* condition. The '+' symbol represents outliers more than 1.5 times the interquartile range away from the minimum (bottom) or maximum (top). (B) Task performance. 1-way ANOVA: $F_{(2,5)} = 0.16$, $p = 0.86$. (C) Pupil size (left panel). 1-way ANOVA: $F_{(2,5)} = 0.23$, $p = 0.80$. Horizontal gaze position (middle panel) is reported here with respect to the letter being the positive direction. The dashed line corresponds to the letter edge. Gaze position across conditions is within 0.23° (1-way ANOVA: $F_{(2,5)} = 1.21$, $p = 0.32$) and not at the letter edge (all $ps < 10^{-6}$). Fixation stability (right panel) quantified as the bivariate contour ellipse area. 1-way ANOVA: $F_{(2,5)} = 0.11$, $p = 0.89$.

Figure S2. Slopes for pRF eccentricity and size versus change in pSFT peak and bandwidth. (A) Box plots for pRF eccentricity vs. change in peak slopes (left panel) and bandwidth slopes (right panel). (B) Box plots for pRF size vs. change in peak slopes (left panel) and bandwidth slopes (right panel). Each box depicts, from bottom to top, the minimum, 25th percentile, median, 75th percentile, and maximum slope. Blue represents values from the *Attend LSF* condition, while red represents values from the *Attend HSF* condition. The '+' symbol represents outliers more than 1.5 times the interquartile range away from the minimum (bottom) or maximum (top). Statistical results reported above each plot were performed at the group level. Bonferroni-corrected p-value *ns* $p > 0.05$. *$p < 0.05$. **$p < 0.01$. ***$p < 0.001$.

Figure S3. pRF size as a function of pRF eccentricity. All points are voxels that survived selection criteria. Each subject has a unique shading in the scatter plots. V1: n = 802, V2: n = 735, V3: n = 398.

Table S1. Group-level results for peak pSFT, pSFT bandwidth, β (BOLD amplitude), and β_0 (BOLD baseline) estimates. *$p < 0.05$.

Table S2. Group-level results for pRF eccentricity vs. change in peak and bandwidth slopes (AMI %/°). Bonferroni-corrected p-value *$p < 0.05$. **$p < 0.01$.

Table S3. Group-level results for pRF size vs change in peak and bandwidth slopes (AMI %/°). Bonferroni-corrected p-value *$p < 0.05$. ***$p < 0.001$.

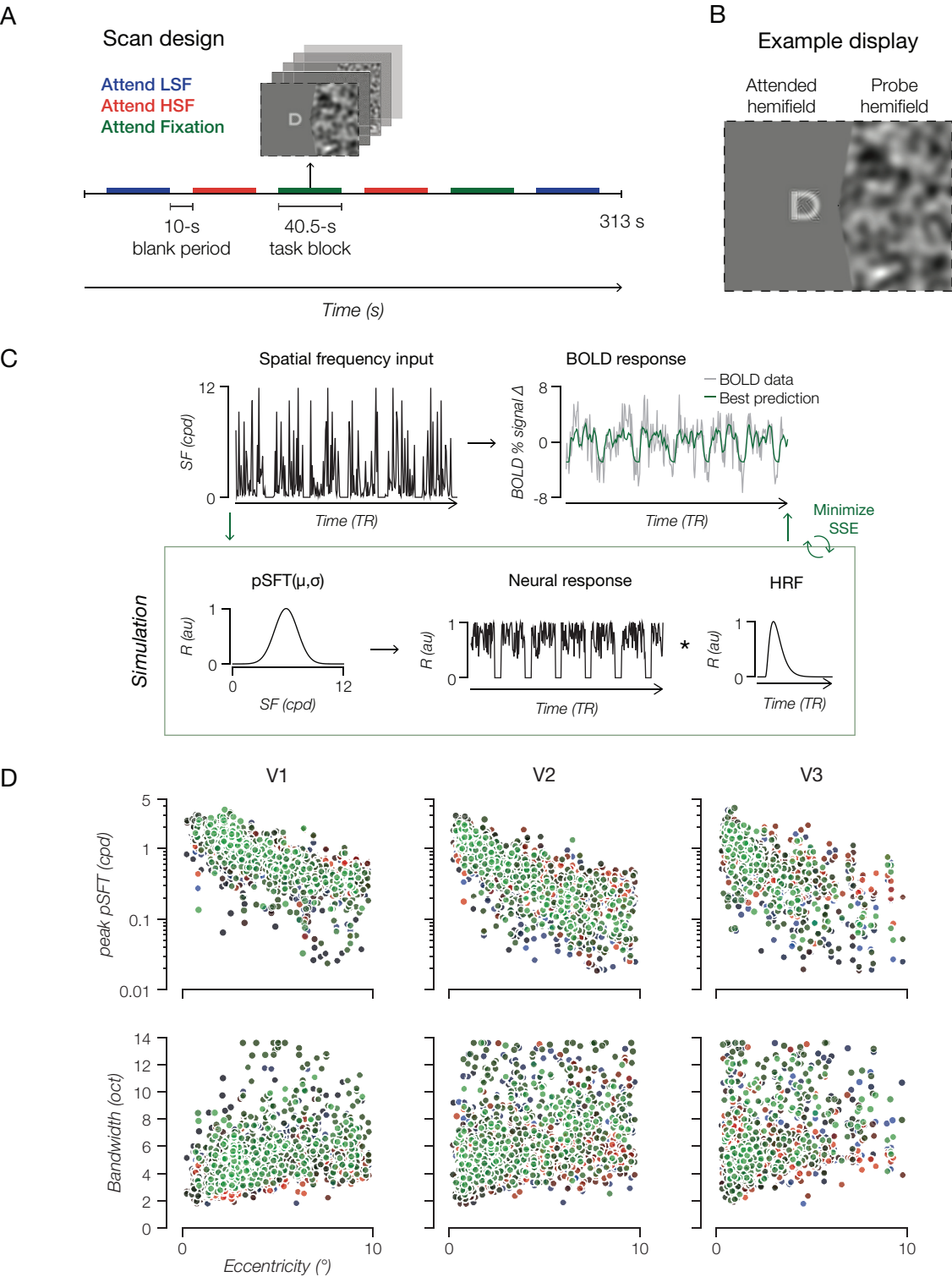
A
Scan design
Attend LSF
Attend HSF
Attend Fixation
10-s
blank period
40.5-s
task block
313 s
Time (s)
B
Example display
Attended
hemifield
Probe
hemifield
C
Spatial frequency input
SF (cpd)
Time (TR)
BOLD response
BOLD data
Best prediction
BOLD % signal Δ
Minimize
SSE
Simulation
pSFT(μ,σ)
R (au)
SF (cpd)
Neural response
HRF
D
V1
V2
V3
peak pSFT (cpd)
Bandwidth (oct)
Eccentricity (°)

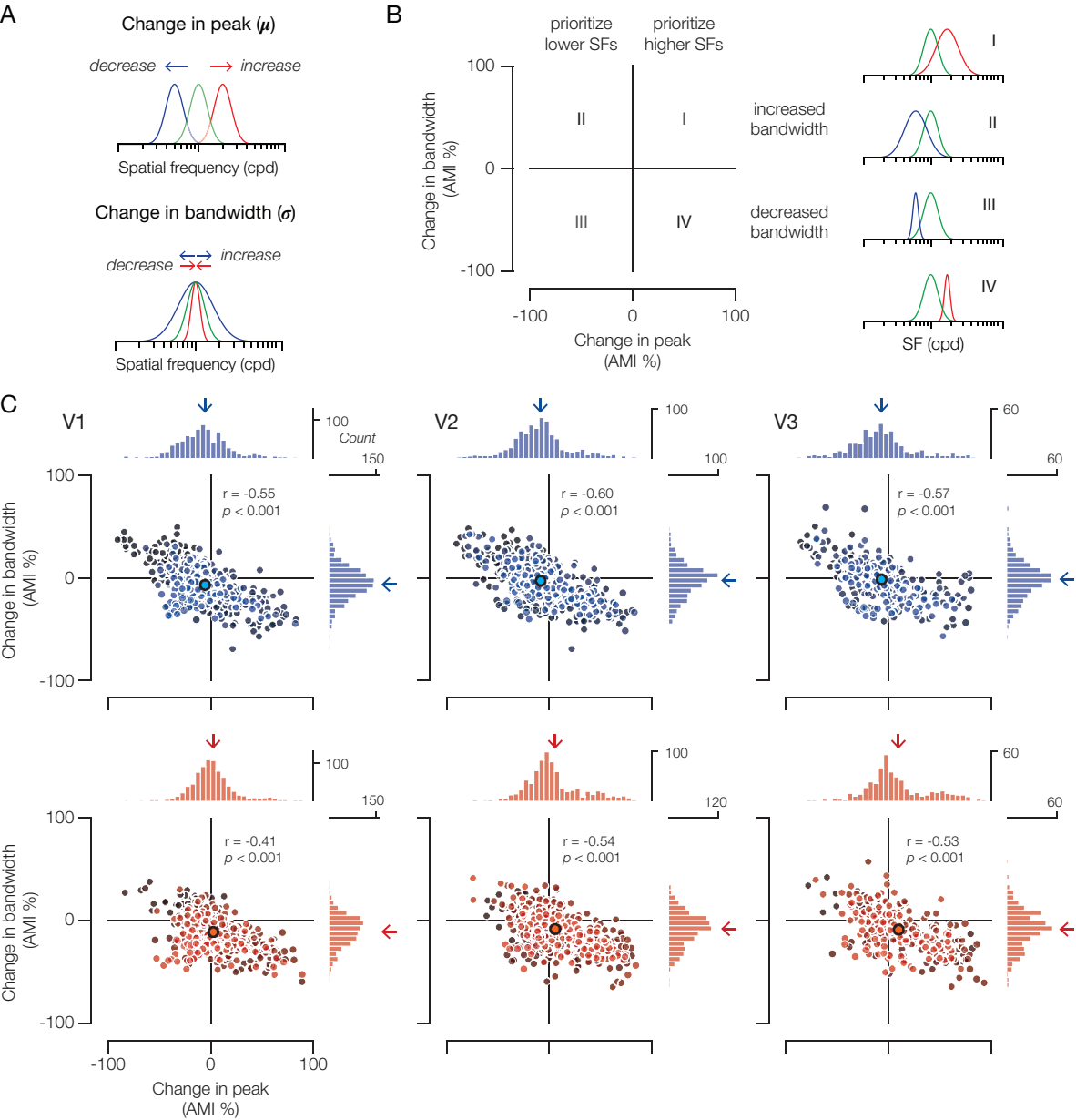
A
Change in peak (μ)
decrease
increase
Spatial frequency (cpd)
Change in bandwidth (σ)
decrease
increase
Spatial frequency (cpd)
B
prioritize lower SFs
prioritize higher SFs
Change in bandwidth (AMI %)
Change in peak (AMI %)
100
0
-100
II
I
III
IV
increased bandwidth
decreased bandwidth
SF (cpd)
C
V1
V2
V3
Count
r = -0.55
p < 0.001
r = -0.60
p < 0.001
r = -0.57
p < 0.001
r = -0.41
p < 0.001
r = -0.54
p < 0.001
r = -0.53
p < 0.001
Change in bandwidth (AMI %)
Change in peak (AMI %)

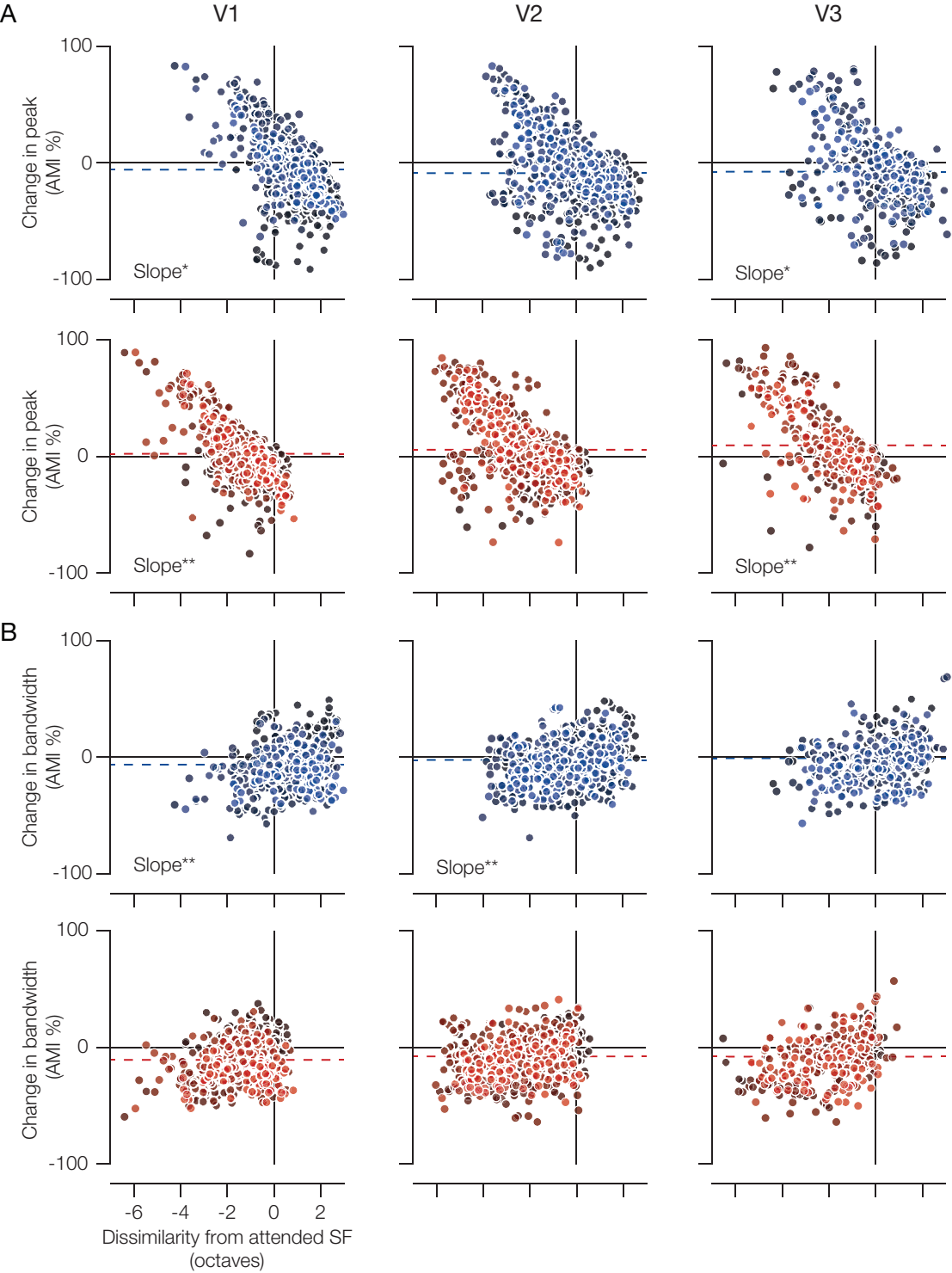
A
V1
V2
V3
Change in peak (AMI %)
100
0
-100
Slope*
Slope**
B
Change in bandwidth (AMI %)
-6
-4
-2
0
2
Dissimilarity from attended SF (octaves)

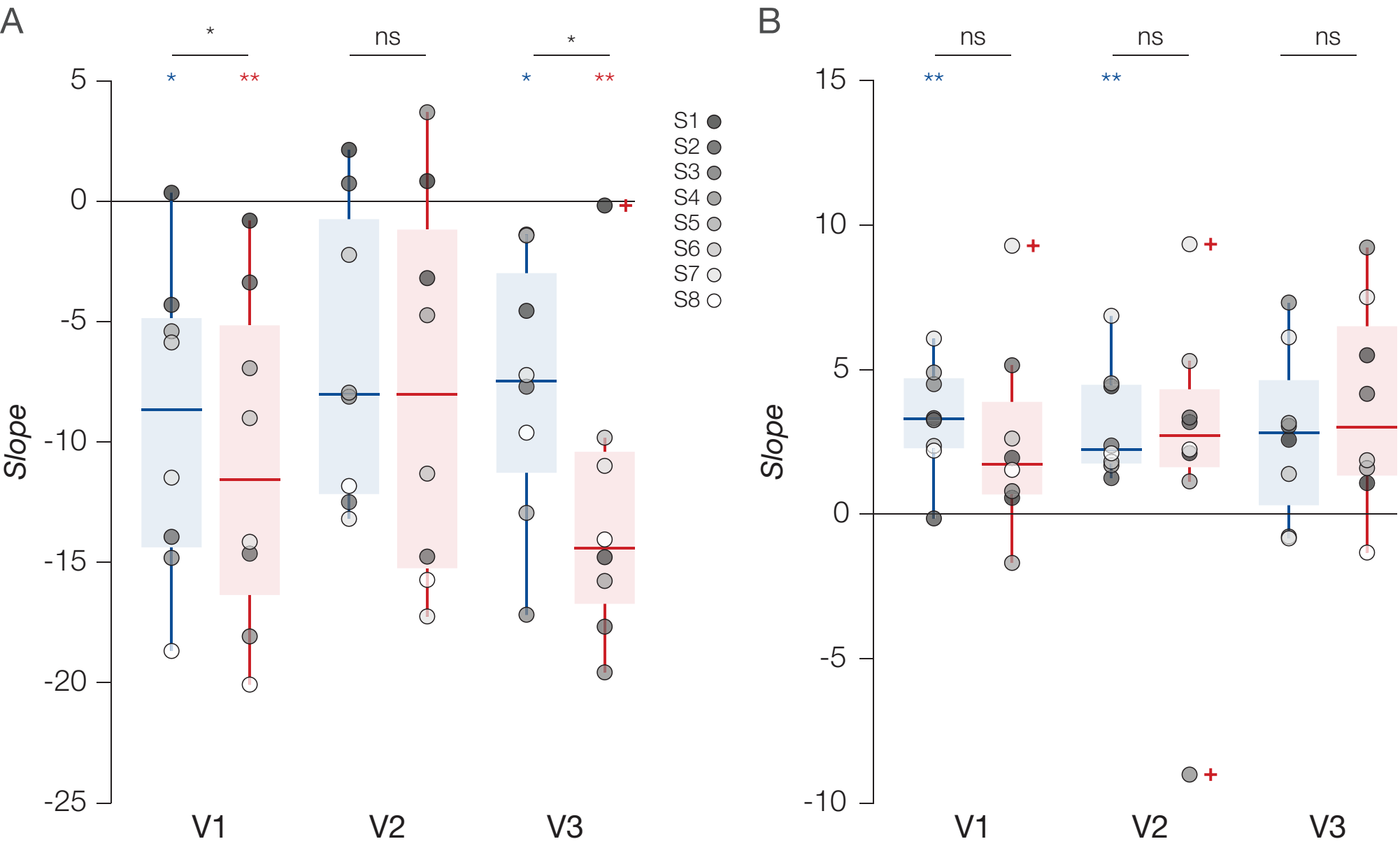
A
B
*
ns
*
ns
ns
ns
*
**
*
**
**
**
S1
S2
S3
S4
S5
S6
S7
S8
Slope
Slope
5
0
-5
-10
-15
-20
-25
15
10
5
0
-5
-10
V1
V2
V3
V1
V2
V3